Rapid #: -20204646

CROSS REF ID: **2150206**

LENDER: **NTE :: Main Library**

BORROWER: **WAU :: Suzzallo Library**

TYPE:	Article CC:CCG
JOURNAL TITLE:	Materials today energy
USER JOURNAL TITLE:	Materials Today Energy
ARTICLE TITLE:	Stability and kinetics enhancement of hydrated vanadium oxide via sodium-ion pre-intercalation
ARTICLE AUTHOR:	Jia, Xiaoxiao
VOLUME:	28
ISSUE:	
MONTH:	
YEAR:	2022
PAGES:	101063-
ISSN:	2468-6069
OCLC #:	

Processed by RapidX: 2/1/2023 3:21:54 PM

Materials Today Energy 28 (2022) 101063

Contents lists available at ScienceDirect

Materials Today Energy

journal homepage: www.journals.elsevier.com/materials-today-energy/

Stability and kinetics enhancement of hydrated vanadium oxide via sodium-ion pre-intercalation

Xiaoxiao Jia [a], Ruixue Tian [b], Chaofeng Liu [a], Jiqi Zheng [a], Meng Tian [a], Guozhong Cao [a, *]

[a] Department of Materials Science and Engineering, University of Washington, Seattle, WA 98195, USA
[b] School of Materials Science and Engineering, Dalian University of Technology, Dalian, Liaoning, 116024, China

ARTICLE INFO

Article history:
Received 11 April 2022
Received in revised form
24 May 2022
Accepted 24 May 2022
Available online 2 June 2022

Keywords:
Aqueous zinc ion batteries
Cathode
Vanadium oxides
Energy storage
Electrochemical kinetics

ABSTRACT

The bilayered vanadium pentoxide (δ-$V_2O_5 \cdot nH_2O$, VOH) is the most promising cathode material for aqueous zinc ion batteries due to its high theoretical capacity, low-cost, and easy preparation. However, the capacity decay arising from the structure instability remains a significant challenge for the application of VOH. The present study focuses on stabilizing the VOH structure via pre-intercalation of Na^+ cations into the bilayers, which occurs by replacing the partial interlayer water. Though has a smaller interlayer spacing, the Na^+ intercalated vanadium oxide (δ-$Na_{0.27}V_2O_5 \cdot 0.7H_2O$, NaVOH) delivers a large specific capacity of 420 mA h/g (at 0.05 A/g), with improved energy efficiency, reversibility, and cycling stability (88% capacity retention after 2000 cycles at 4 A/g), in comparison to those of $V_2O_5 \cdot 1.0H_2O$. The results reveal that Na^+ions are favorably intercalated within the VOH layers by the spontaneous ion-exchange with structural water. The introduction of sodium cations, an increased amount of V^{4+}, as well as a reduced interlayer water content in NaVOH collectively result in the fast transport and reaction kinetics as well as the improved structural and electrochemical stability.

1. Introduction

The rapidly-growing energy consumption and the big shift from traditional fossil fuel to the renewable energy demand safe, reliable, efficient, and cost-effective energy storage technologies [1,2]. Aqueous rechargeable batteries (ARBs) appear to be a very promising solution [3,4]. Compared with their organic counterparts, ARBs show advantages in terms of non-toxicity, low-cost, eco-friendliness, ease of handling, high-safety, and high ionic conductivity (10^{-1}–10 S/cm *vs.* 10^{-3}–10^{-2} S/cm for organic electrolytes) [5]. Among various ARBs, aqueous zinc ion batteries (ZIBs) have stood out on account of the unique merits of zinc metal anode, including the high zinc abundance (Zn: 79 ppm, Li: 17 ppm in the Earth's crust), a high theoretical volumetric capacity (5855 mA h cm^{-3} compared to 2061 mA h cm^{-3} for lithium and 1129 mA h cm^{-3} for sodium), and relatively low redox potential (−0.76 V *vs.* standard hydrogen electrode) [5,6]. One of the biggest obstacles that hinders the development of aqueous ZIBs is the sluggish Zn^{2+} ion transport in cathode materials, arising from the large atomic mass and divalent state of Zn ions [7]. This can be detrimental to both the reversibility of the redox reactions and the structure stability of cathode materials, resulting in the unsatisfactory cycling stability and rate performance, as well as the inadequate energy efficiency of the ZIBs [5,6].

A wide range of cathode materials have been explored for their zinc ion storage capabilities. Manganese oxides can provide a high specific capacity of 300 mA h/g but suffer from poor cycling stability due to active materials dissolution and significant structural variation [8,9]. Prussian blue and its analogues show a high operating voltage but exhibit a very limited specific capacity (<100 mA h/g) [10,11]. Organic redox-active compounds, the promising cathode materials for the flexible solid state ZIBs, demonstrate low electronic conductivities and poor rate capabilities [12,13]. Currently, increasing research efforts have been devoted to the materials with two-dimensional layered structures, which can enable fast charge carrier diffusion, like vanadium-based [14–20] and dichalcogenide-based materials [21,22]. Layered vanadium pentoxide (V_2O_5) is, now the most promising cathode candidates for aqueous ZIBs as they can undergo multielectron transfer, leading to a high theoretical capacity of 589 mA h/g (with two-electron transfer from V^{5+} to V^{3+}), and their open structure enables facile ion transport [6,23]. Among V_2O_5 and its derivations, the hydrated vanadium oxide δ-$V_2O_5 \cdot nH_2O$ is particularly promising due to its expanded interlayer

* Corresponding author.
E-mail address: gzcao@uw.edu (G. Cao).

https://doi.org/10.1016/j.mtener.2022.101063
2468-6069/

spacing (~11.5 Å), mixed valence states (V^{5+} and V^{4+}), and the fast ion-exchange capability [24,25]. The bilayered δ-$V_2O_5{\cdot}nH_2O$ is formed by two layers of [VO_x] polyhedra, which are separated and stabilized by the interlayer water molecules [26]. A high specific capacity of δ-$V_2O_5{\cdot}nH_2O$ has been demonstrated in the aqueous ZIBs; when cycled in the voltage range of 0.2−1.6 V vs. Zn/Zn^{2+}, δ-$V_2O_5{\cdot}nH_2O$ can deliver a specific capacity of ~300 mA h/g at 0.5 mA/g [27−29]. Over prolonged cycling, however, an obvious capacity fading is observed due to the gradual loss of stacking order of the V−O layers upon intercalation/deintercalation of charge carriers [30]. Increasing the electrochemical stability is, therefore, the prerequisites needed to realize the practical utilization of δ-$V_2O_5{\cdot}nH_2O$ cathode materials in aqueous ZIBs.

Pre-intercalation of foreign ions is, by far, the most effective and facile strategies to stabilize the layered structure [31]. Numerous species have been studied to tune the interlayer spacing and chemical composition of δ-$V_2O_5{\cdot}nH_2O$, including alkali (Li^+, Na^+, K^+), alkali earth (Ca^{2+}, Mg^{2+}), transition metal (Ag^+, Co^{2+}, Cu^{2+}, Zn^{2+}), and other ions or groups (NH_4^+) [27−29,32,33]. Compared to the pristine δ-$V_2O_5{\cdot}nH_2O$ phase (VOH), the metal ion-preintercalated vanadium oxides (MVOH) exhibit higher specific capacities and better capacity retention [27−29,32,33]. Most of the studies attributed the better performance of MVOH to the enlarged lattice spacing and the pillar effect of the pre-introduced metal ions [32,33]. Some work, however, contradicted this explanation by demonstrating a high zinc ion storage capacity and improved cycling stability with a reduced interplanar space by pre-inserting cations such as K^+ [28]. Although pre-intercalation strategy has been widely used, factors that determine the interlayer spacing of MVOH and reasons that are responsible for the optimized Zn^{2+} in storage properties have not been systematically investigated.

In the present study, the Na-preintercalated δ-V_2O_5 (δ-$Na_{0.27}V_2O_5{\cdot}0.7H_2O$, NaVOH) and the pristine δ-$V_2O_5{\cdot}1.0H_2O$ (VOH) were synthesized via hydrothermal growth. Na^+ ions can be intercalated into VOH structure by easily replacing some interlayer water molecules, which decreases the interplanar distance from 12.0 Å (VOH) to 11.0 Å (NaVOH) but preserves the bilayered structure. Our results reveal that the lattice spacing between vanadium oxide layers can be correlated to not only the interlayer water content but also the electronegativity and hydrated radius of the preintercalated cations. Despite its narrower interlayer spacing, NaVOH exhibits a much faster Zn^{2+} diffusion rate (D_{Zn}^{2+}~10^{-9}) than that of VOH (D_{Zn}^{2+}~10^{-10}). When being used as the cathode materials for the aqueous ZIBs, NaVOH demonstrates a specific capacity of 420 mA h/g at 50 mA/g, higher than that of VOH (324 mA h/g at 50 mA/g), an improved energy efficiency with a highly reversible Zn^{2+} intercalation/deintercalation, and a better electrochemical stability (88% capacity retention compared to 43% for VOH after 2000 cycles at 4 A/g). Electrochemical properties of the metal cation-intercalated vanadium oxides depend on a synergistic effect of many factors, including the types of the introduced cations, the amount of tetravalent vanadium ions, and the content of interlayer water, rather than the interlayer distance alone. Here, the influence of the preintercalated cations on the interplanar spacing, structural stability, as well as the electrochemical performance of the electrodes was investigated. The underlying cation-exchange mechanism in δ-$V_2O_5{\cdot}nH_2O$ and the interplay between the interlayer water and the intercalated metal cations was discussed.

2. Results and discussion

2.1. Crystal structure, microstructure, and composition

The scanning electron microscopy (SEM) image (Fig. 1a) shows that NaVOH has a highly interweaved foam-like architecture, built from ultrathin nanoribbons. In the high-resolution transmission electron microscopy image of NaVOH, a set of lattice fringes with an interplanar spacing of 2.17 Å (Fig. 1b) is observed, which corresponds to the (005) planes of NaVOH and agrees well with the peak at 41.1° from X-ray diffraction (XRD) (d_{005} = 2.19 Å). Another set of lattice fringes, which are perpendicular to that of (005) planes, shows an interplanar spacing of 1.96 Å and corresponds to the spacing of (510) plane of NaVOH. The TEM-energy dispersive spectroscopy (EDS) elemental mapping images (Fig. 1c) reveal the homogenous distribution of the Na, V, and O in the NaVOH nanoribbons, confirming the successful introduction of Na ions in the VOH. From the EDS spectra of NaVOH, the absence of sulfur peaks (S) confirms that all unreacted Na_2SO_4 salts was removed upon washing and centrifuging. All sodium here is the chemically preintercalated Na^+ions in NaVOH. The Na:V ratio in NaVOH is estimated to be 1:7.5, with a chemical formula of δ-$Na_{0.27}V_2O_5{\cdot}nH_2O$.

Fig. 1d shows the XRD patterns of NaVOH and VOH. The diffraction peaks of VOH could be well indexed to the standard $V_2O_5{\cdot}1.6H_2O$ pattern (JCPDS No.40-1296) [32]. The pronounced (00*l*) diffraction peaks of two samples indicate a typical layered structure along *c*-axis. The structure of hydrated vanadium pentoxide has double V_2O_5 sheets, which is constructed by the square pyramidal [VO_5] units and the octahedral [VO_6] units, and contains interlayer guest cations/water molecules (as shown in the inset of Fig. 1d) [34]. NaVOH exhibits almost the same characteristic peaks as that of VOH, suggesting that the bilayered structure of VOH is well-preserved after the introduction of Na^+ cations. The (001) peak of NaVOH ($2\theta = 8.1°$) shifts toward a higher degree comparing to that of VOH (2θ = 7.3°), which corresponds to a decreased interlayer spacing of NaVOH (NaVOH: 11.0 Å, VOH: 12.0 Å). This is different from most work reported that pre-inserting metal ions enlarges the interplanar spacing of $V_2O_5{\cdot}nH_2O$ [14,17,35], with the exception of K^+ [28]. The exact parameter(s) and mechanism determine the variation of interlayer spacing of hydrate vanadium pentoxide are not clear and obviously require further study. As pre-inserted ions are serving as charge carriers but remain chemically inert, valence states and ionic radius are likely the first characteristics to be considered. Literature data and our prior and current results revealed no coherent correlation between the interlayer spacing and ionic radius or valence states of pre-inserted cations. Table 1 compares and summarizes the structural and composition data of various $M_xV_2O_5{\cdot}nH_2O$ materials (M = Na, K, Mg, Al), the interlayer spacing of $M_xV_2O_5{\cdot}nH_2O$ can be correlated to both the hydrated radius and the electronegativity of pre-inserted cations. As shown in Fig. 2 and Table 1, a larger hydrated ion radius leads to a bigger interlayer spacing of $M_xV_2O_5{\cdot}nH_2O$, but not the anhydrous ionic radius. Also, a smaller electronegativity of M cation leads to a smaller interlayer spacing due to a stronger electrostatic attraction force between M cations and O anions pulling adjacent V−O layers closer.

Raman spectra of NaVOH is very similar to that of VOH (shown in Fig. 1e) and the assignment of the observed modes is given in Table S1. For VOH, the highest frequency mode at 1025 cm^{-1} is attributed to the stretching of the strongest V]O bonds in [VO_5]; the bending of those V]O bonds occurs at around 265 and 424 cm^{-1} [39,40]. The peak at 898 cm^{-1} in VOH is characteristic of the V−OH_2 stretching vibration [41]. The corresponding mode in NaVOH exhibits a much decreased intensity, suggesting a reduced amount of interlayer water in NaVOH. This is supported by the peak at 353 cm^{-1}, which is attributed to the lattice water vibration [41]. The peak at 709 cm^{-1} for VOH originates from the stretching vibration of V_2−O bonds (doubly coordinated oxygen) [39], whereas the one located at 671 cm^{-1} corresponds to those disordered V_2−O [42]. Such split peak was not observed in NaVOH. Only a single broad

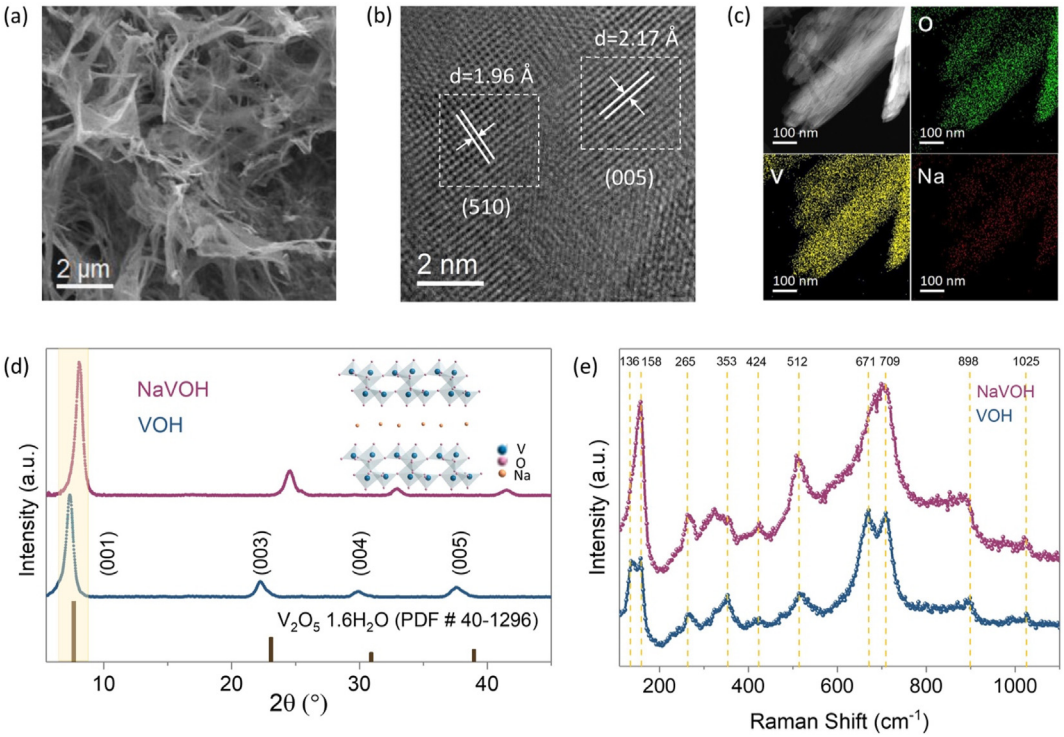

Fig. 1. (a) SEM image, (b) HR-TEM image, and (c) TEM image with the corresponding EDS elemental mappings of NaVOH. (d) XRD patterns of NaVOH and VOH, with a schematic diagram of the NaVOH crystal structure (inserted). (e) Raman spectra of NaVOH and VOH. EDS, energy dispersive spectroscopy; HR-TEM, high-resolution transmission electron microscopy; SEM, scanning electron microscopy; TEM, transmission electron microscopy; XRD, X-ray diffraction.

Table 1
Correlation between properties of the chemically preintercalated M cations (size, electronegativity) and the structure and composition of $M_xV_2O_5 \cdot nH_2O$ materials.

Preintercalated M cation	None	Na	K	Mg	Al
Ionic radius (Å) [36,37]	–	0.95	1.33	0.65	0.53
Hydrated ion radius (Å) [36,37]	–	3.58	3.31	4.40	4.80
Interplanar spacing (Å)	12.0	11.0	9.9	13.2	13.4
Electronegativity of element (Pauling scale) [38]	–	0.93	0.82	1.31	1.61
Electronegativity difference (O: 3.44)	–	2.51	2.62	2.13	1.83
M: V	–	1:7.5	1:12	1:12.5	1:11
Amount of V^{4+} (%)	9.1%	12.1%	20%	16.5%	23.0%
	(This work)	(This work)	[28]	[27]	[29]

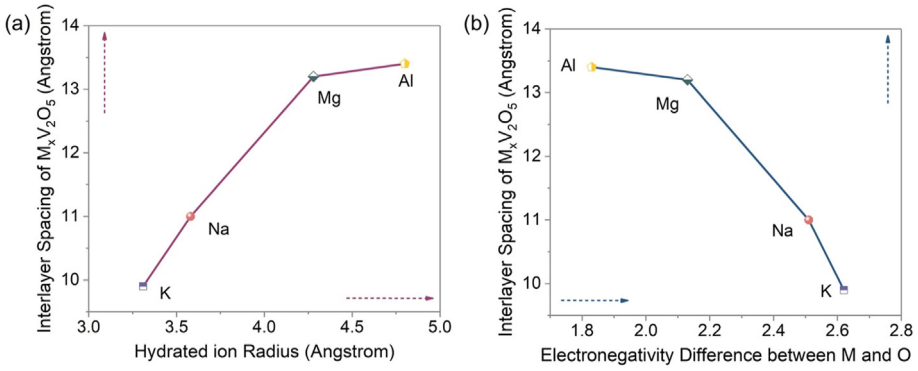

Fig. 2. The relationship between interlayer spacing of $M_xV_2O_5 \cdot nH_2O$ with respect to the (a) radius of the hydrated M cation and (b) the electronegativity difference between M and oxygen.

peak was detected at 699 cm^{-1}, suggesting a more ordered vanadium oxide structure due to Na^+ introduction [28,43]. The peak at 512 cm^{-1} is assigned to the V_3–O (triply coordinated oxygen) stretching vibration [44]. The low-frequency peak at 158 cm^{-1} is associated with the bending vibration of –V–O–V–O– chains [28,39]. VOH exhibits one additional peak at 136 cm^{-1}, which

comes from the chain vibration subjected to the compressive deformation along ***a*** direction [45].

Thermal stability and hydration degree (n in δ-$Na_xV_2O_5 \cdot nH_2O$) of the samples were examined by simultaneous thermogravimetry analysis (TGA) and differential scanning calorimetry (DSC) analysis. Fig. 3a shows there are weight losses with an increasing temperature, attributing to two kinds of interlayer water in $V_2O_5 \cdot nH_2O$. One is that leaves at 120 °C; this is the physically adsorbed and weakly bound water, the amount of which is determined by the water pressure in the environment. The other type leaves at 250 °C, which corresponds to the water that chemically and tightly bonded to the vanadium oxide network [26,46,47]. According to the weight loss during the two stages, the corresponding water removal process for NaVOH and VOH can be expressed as follows:

$$Na_xV_2O_5 \cdot 0.7H_2O \xrightarrow{120^\circ C} Na_xV_2O_5 \cdot 0.07H_2O \xrightarrow{250^\circ C} Na_xV_2O_5$$

$$V_2O_5 \cdot 1.0H_2O \xrightarrow{120^\circ C} V_2O_5 \cdot 0.38H_2O \xrightarrow{250^\circ C} V_2O_5$$

Overall, the H_2O content of NaVOH and VOH is estimated to be $n = 0.7$ and $n = 1.0$, respectively. This number is smaller than that in $V_2O_5 \cdot 1.6H_2O$ ($n = 1.6$), as the samples were heated to 120 °C for 2 h prior to the TGA test. A smaller amount of water situated between the bilayers in NaVOH explains its narrower interlamellar spacing than that of VOH. A sharp exothermic DSC peak is observed at ~350 °C for both VOH and NaVOH, which corresponds to the crystallization of the orthorhombic V_2O_5 due to some local reorganizations [48]. The DSC curve of VOH showed a sharp endothermic peak at 679 °C, which is assigned to the melting of V_2O_5. It is found that the decomposition of NaVOH does not start within the range of testing temperature, suggesting its better thermal stability than VOH. From the temperature range of 120–200 °C, it can be estimated that the two samples have the same amount of physically adsorbed H_2O per V_2O_5 ($n = 0.62$) because they were synthesized under the same H_2O vapor pressure. In the second phase (250–400 °C), notably, for VOH, the mass loss is about 3.6%, corresponding to $n = 0.38$ water bonded to the vanadium oxide network. The weight loss of NaVOH during this stage, however, is very limited, suggesting a negligible amount of chemically bonded water in NaVOH (only ~0.07). This probably arises from the replacement of structural water by the intercalated foreign cations (Na^+ ions in our case). According to Livage et al. [46,49], when water molecules is adsorbed between bilayers, surface hydroxyl groups could be easily involved in the acid dissociation reactions to produce solvated protons ($-V-OH + H_2O \rightarrow -V-O^- + H_3O^+$). These acid protons ($H_3O^+$) tend to move along the bilayer surface and can be easily replaced by the other cations or molecules, endowing VOH with ion-exchange properties. Our thermogravimetric results (Fig. 3a) reveal that approximately 0.31 water per V_2O_5 was removed when Na^+ions were preintercalated. This value is in line with the literature data that there is $0.3H_3O^+$ per V_2O_5, and the exchange capacity of $V_2O_5 \cdot nH_2O$ with respect to the monovalent metal cations is about 0.3 [46,50]. The X-ray photoelectron spectroscopy (XPS) survey spectrum (Fig. 3b) reveal the embedment of Na^+ into the lattice of NaVOH, where a clear Na 1*s* spectrum is detected at 1071.5 eV. The V $2p_{3/2}$ spectra reveal a mixed V^{5+} and V^{4+} valence states in both NaVOH and VOH samples (Fig. 3c). The peak centered at a higher binding energy of 517.4 eV was ascribed to the oxidation state of V^{5+}, while a lower binding energy of 516.3 eV was assigned to V^{4+} [32,51]. The molar ratio of V^{4+}/V^{5+} is determined to be 1:7 in NaVOH and 1:10 in VOH, suggesting an average oxidation state of $V^{4.88+}$ and $V^{4.91+}$ for NaVOH and VOH, respectively. The results of XPS confirm the increased concentration of lower valent vanadium in NaVOH.

To verify the feasibility of Na^+ pre-intercalation in VOH and its substitution of interlayer water, we performed the first-principals calculations based on the density functional theory. The

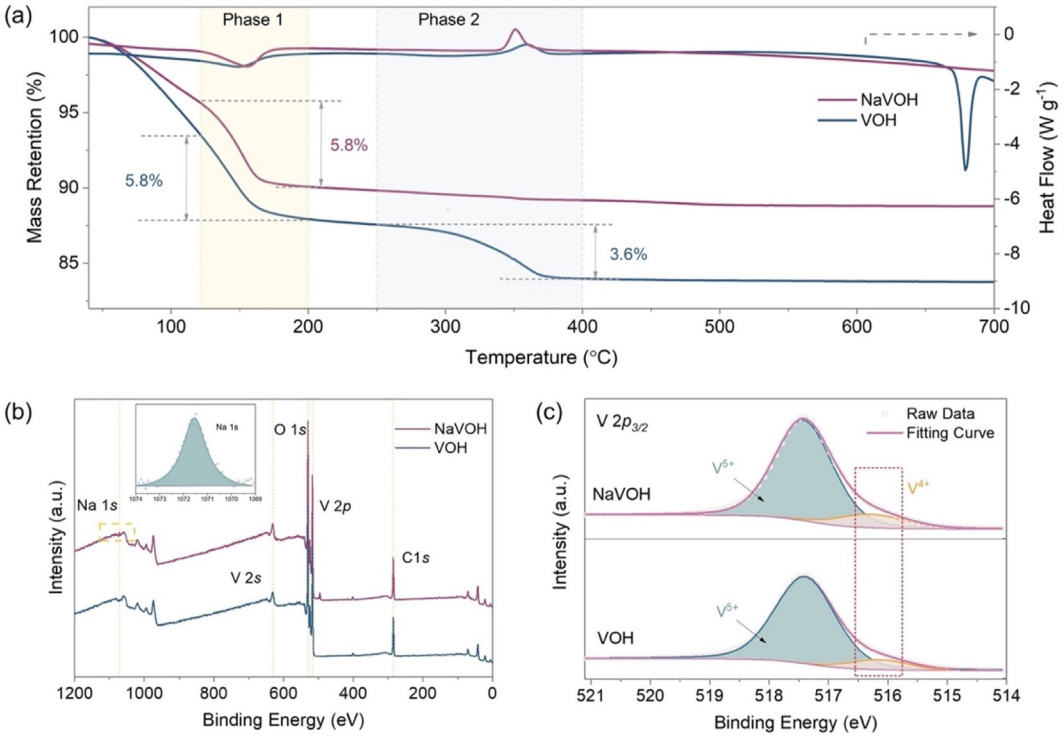

Fig. 3. (a) TGA/DSC curves of NaVOH and VOH within 30–700 °C. (b) XPS survey spectra, high resolution of Na 1*s* spectra (inserted) and (c) V $2p_{3/2}$ spectra collected from NaVOH and VOH. DSC, differential scanning calorimetry; TGA, thermogravimetric analysis; XPS, X-ray photoelectron spectroscopy.

computational details can be found in the **SI**. In $V_2O_5 \cdot nH_2O$, due to the strong polarizing power of V^{5+}, the coordinate water molecules can undergo acid dissociation reactions on the interlayer surface ($[V(OH_2)_6]^{5+} + hH_2O \Rightarrow [V(OH)_h(OH_2)_{6-h}]^{(5-h)+} + hH_3O^+$), leading to the formation of H_3O^+ ions [46,50,52]. In the calculation model of VOH, there is one H_3O^+ per five H_2O [26]. For the calculations of NaVOH, we replaced one of the H_3O^+ in VOH with one Na atom. The optimized lattice parameters of the VOH and NaVOH structure demonstrate that the interlayer distance (lattice parameter *c*) slightly decreases after Na^+ insertion (as summarized in Table S2), which agrees well with the XRD results of our samples. The formation energy of replacing one H_3O^+ with one Na^+ is calculated to be −0.46 eV, thus confirming that the pre-intercalation of Na^+ ions into VOH is an energetically favorable/spontaneous process. A lower energy of NaVOH also suggests its enhanced thermal stability. This is supported by the TGA results that the decomposition of VOH starts at 679 °C, while that of NaVOH does not occur in the range of our testing temperature (30−700 °C). The total density of states of NaVOH and VOH (Fig. 4a) show that, substituting one H_3O^+ with one Na^+shifts the conduction bond to the left toward the Fermi level. The reduced band gap of NaVOH means the easier excitation of electrons to the conduction band, indicative of an improved electronic conductivity of NaVOH. The bonding interactions between Na^+ and VOH can be seen from the projected density of states (Fig. 4b). The overlap between the electronic states of Na and the V and O atoms demonstrates the covalent hybridization interactions between inserted Na and the VOH structure. The charge density difference was then calculated to clarify the bonding nature of Na with the adjacent atoms in NaVOH. As shown in Fig. S1, there is a depletion of electron density (blue region) around Na and an enrichment of electron density (yellow region) around V and O. This indicates the obvious charge transfer between Na and the surrounding atoms, revealing the formation of ionic bonds between the inserted Na and the host. Quantitatively, the Bader charge analysis confirms there is ~0.9 |e| transferred from Na to the nearby V and O, demonstrating that Na is strongly ionized. In summary, the density functional theory results show that, by replacing water (H_3O^+) in the interlayer space, the intercalation of Na ions in VOH is thermodynamically favorable and is accompanied by an improved thermostability and electronic conductivity. In addition, strong chemical bonds (predominantly ionic) will form between Na and the VOH structure, contributing to the enhanced host structure stability. These results confirm the Na^+ replacing water mechanism, clarify the benefits of Na^+ pre-intercalation, and help explain the origin of the better Zn^{2+} storage performance in NaVOH.

2.2. Electrochemical properties and battery performance

The Zn^{2+} storage performance of NaVOH and the role of pre-intercalated Na^+ ions were evaluated by assembling CR 2032 coin cells using 3 M $Zn(CF_3SO_3)_2$ aqueous solution as the electrolyte and Zn metal foil as the anode. Fig. 5*a* shows the initial three cyclic voltammetry (CV) profiles of Zn//NaVOH cells tested within the voltage range of 0.2−1.6 V (vs. Zn^{2+}/Zn) at a scan rate of 0.1 mV/s. Two pairs of well-defined redox peaks are observed at around ~1.0 and 0.5 V, which are ascribed to the redox reactions between V^{5+}/V^{4+} and V^{4+}/V^{3+} pairs, respectively [20,27]. The well overlapped CV profiles for the first three cycles suggest a highly reversible electrochemical Zn^{2+} insertion/extraction process in NaVOH. For comparison, the 3rd cycle of CV curves for NaVOH and VOH are shown in Fig. 5*b*. They exhibit similar shapes and have peaks at the similar positions, indicating that the redox reactions during the electrochemical Zn^{2+} ion intercalation/deintercalation are the same for both materials. The difference between two samples is that NaVOH possess a larger current response and a larger integrated area of CV curves in comparison to that of VOH (as summarized in Table 2), indicating a larger capacity of NaVOH. Also, the smaller voltage gaps between each pair of redox peaks of NaVOH than those of VOH reflect the lower polarization, a better reversibility, thus the better electrochemical kinetics of NaVOH electrodes. Fig. 5c compares the galvanostatic discharge (Zn^{2+} insertion) and charge (Zn^{2+} extraction) (GCD) curves of NaVOH and VOH at a current density of 0.05 A/g. Both NaVOH and VOH display two pairs of charge/discharge plateaus (1.1−0.9 and 0.7−0.4 V), which agree well with the two pairs of redox peaks shown in CV curves (Fig. 5b). For NaVOH, the potential gap between the charge/discharge plateaus is smaller than that of VOH, also in good agreement with the narrower peak separation from the CV curves. In the 1st cycle, NaVOH delivers an initial discharge capacity of 420 mA h/g, much higher than that of VOH (324 mA h/g). After 50 cycles, the GCD curve of NaVOH remains almost unchanged, while VOH shows an obviously enlarged overpotential and a significant capacity decay, indicating a more reversible Zn^{2+} intercalation/deintercalation and better cycling stability of NaVOH.

Rate responses of NaVOH and VOH are compared in Fig. 5d. The discharge capacities of Na-pre-inserted V_2O_5 at 0.5, 1.0, 2.0, 4.0, and 8.0 A/g are 395, 375, 348, 310, and 262 mA h/g, respectively. Even when the current density increases to 8.0 A/g, it still delivers a high reversible capacity of 262 mA h/g, achieving a capacity retention of 66% (with respect to the capacity at 0.5 A/g). When the rate returns to 0.5 A/g, a reversible capacity of 385 mA h/g can be recovered, indicating a good structure stability and the high electrochemical reversibility of NaVOH. The VOH cathode, in comparison, supplies a

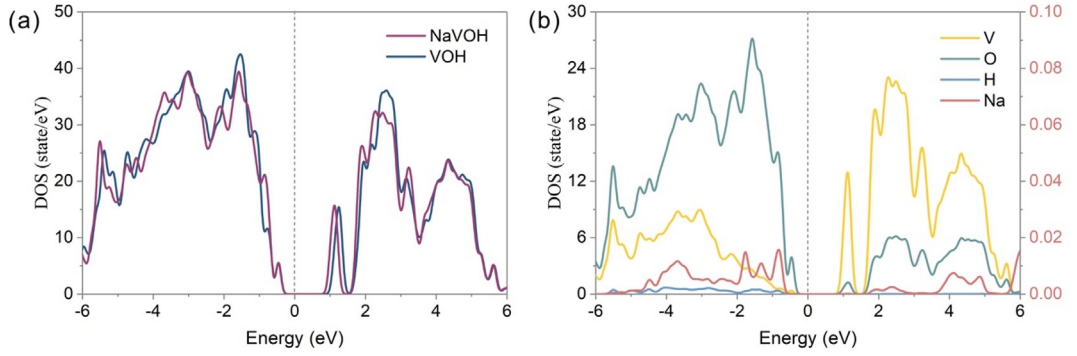

Fig. 4. (a) The total density of states of VOH and NaVOH. (b) The projected density of states of NaVOH, the left axis (black) is the density of states of V, O, and H atoms, the right axis (pink) is the density of states of the Na atom. The Fermi energy has been shifted to zero, denoted by the dotted line.

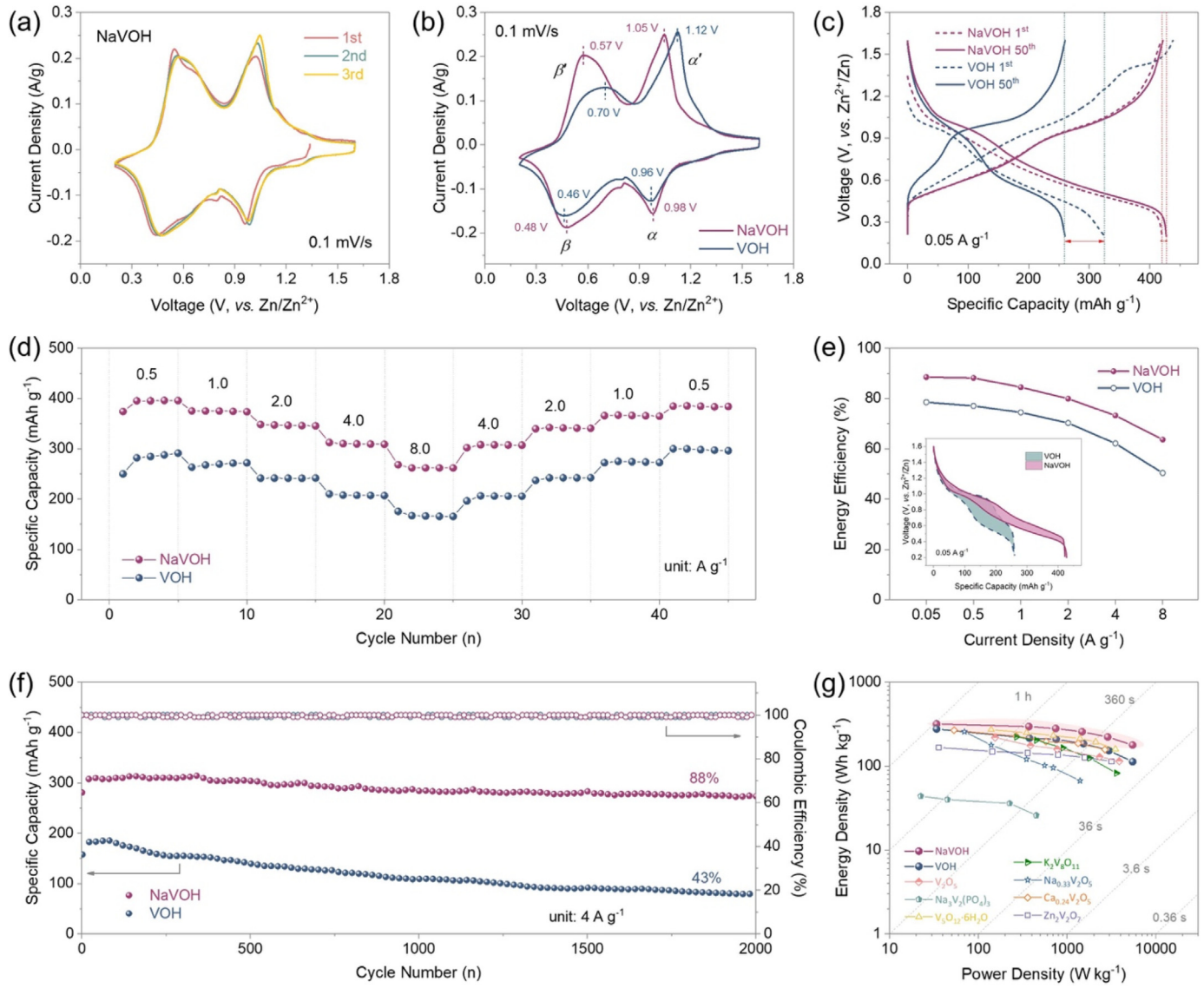

Fig. 5. Electrochemical characterizations of the aqueous Zn//3 M $Zn(CF_3SO_3)_2$//NaVOH and Zn//3 M $Zn(CF_3SO_3)_2$//VOH cells. (a) The initial three cycles of CV curves for NaVOH at a scan rate of 0.1 mV/s. (b) CV curves of NaVOH and VOH at 0.1 mV/s (c) The 1st and 50th galvanostatic charge/discharge curves at a current density of 0.05 A/g. (d) Rate capability. (e) Rate capability evaluated in terms of energy efficiency, insert figure: a comparison of the voltage hysteresis of two samples at 0.05 A/g, the area enclosed by the charge/discharge profile represents the energy loss. (f) Long-term cycling stability at 4.0 A/g. (g) Ragone plots of the aqueous Zn//NaVOH and Zn//VOH cells and the aqueous ZIBs with other reported vanadium-based cathode materials. Noted that the energy density values are based on the mass of the active materials in cathode.

Table 2
A comparison of the peak positions and potential gaps between redox pairs of NaVOH and VOH.

Sample	Redox pairs (V)	Peak voltages (V)	Peak separation (V)	Central position (V)
VOH	V^{5+}/V^{4+}	0.96/1.12	0.16	1.04
	V^{4+}/V^{3+}	0.46/0.70	0.24	0.58
NaVOH	V^{5+}/V^{4+}	0.98/1.05	0.07	1.02
	V^{4+}/V^{3+}	0.48/0.57	0.09	0.52

smaller capacity than that of NaVOH at all current densities, and it has only 57% capacity retention when the current density increases from 0.5 to 8.0 A/g. Besides specific capacity/energy, another critical factor to be considered for the large scale energy storage application is energy efficiency, which is defined as the ratio of the discharged energy density to the charged energy density [53]. As presented in Fig. 5e, at a current rate of 0.05 A/g, the energy efficiency of NaVOH is 88%, much higher than that of VOH (78%), and this value drops slightly for NaVOH (64%) while rapidly for VOH (50%) when the current rate increases to 8.0 A/g, again revealing the higher reversibility and faster kinetics of Zn^{2+} insertion/extraction in NaVOH. The long-term cycling performance of the Zn//NaVOH and Zn//VOH cells were evaluated at a high current density of 4.0 A/g (Fig. 5f). The discharge capacity of NaVOH gradually increases in

the initial 150 cycles and stabilizes at 310 mA h/g. After 2000 cycles, a high specific capacity of 274 mA h/g can still be maintained for NaVOH (with a capacity retention of 88%). This is much higher than that of VOH, whose specific capacity decreases sharply from 186 mA h/g to 79 mA h/g with a capacity retention of only 43%.

NaVOH samples show good performance in both rate capability and cycling stability compared with that of VOH, which can be attributed to the substitution of partial interlayer water by Na^+ ions and the introduction of more tetravalent vanadium in NaVOH. Interlayer Na^+ ions can form stronger chemical bonds with the V—O framework than interlayer water molecules, which helps to better maintain the layered structure during cycling. The presence of more V^{4+} can facilitate the electronic hopping between V^{4+} and V^{5+} and weaken the electrostatic interactions between carrier ions and the host lattice. Both factors are beneficial to the ionic and electronic diffusion and contribute to a suppressed structural distortion during the repeated Zn^{2+} intercalation and deintercalation. In addition to the improved rate and cycling performance, the aqueous Zn//NaVOH cell also realizes an energy density of 295 Wh/kg (at a power density of 372 W/kg) and a power density of 5477 W/kg (at the energy density of 178 Wh/kg), which is not only superior than VOH but also outperform many cathode materials for the aqueous ZIB systems (as illustrated in the Ragone plots in Fig. 5g) [14—18] NaVOH with a narrower interlayer spacing achieves a larger specific capacity, higher energy efficiency, longer cycling stability, and better rate capability than the pristine VOH, which arise from the low amount of interlayer water, high content of V^{4+} ions, and the strong bonding between the interlayer Na^+ions and the vanadium oxide network.

The *ex-situ* XRD, XPS, TEM, and SEM were carried out to study the structure variation of NaVOH during the Zn^{2+} ion intercalation/deintercalation processes. Fig. 6a shows the *ex-situ* XRD patterns of NaVOH after the initial discharging and charging. After being discharged to 0.2 V, the (001) peak shifts from the pristine state (8.14°) to a lower degree (6.5°), corresponding to an interlayer expansion from 11.0 Å to 13.7 Å with Zn^{2+} ion insertion. After the subsequent charging to 1.6 V, the (001) peak shifts back to the original position associated with Zn^{2+} extraction. In addition, the (003), (004), and (005) peaks all present the similar shifting process upon cycling, indicating a highly reversible Zn^{2+} intercalation/deintercalation in NaVOH. Also, it can be observed that the original layered structure of NaVOH is well-preserved during cycling, suggesting its good structure stability. Fig. 6b is the high resolution XPS spectra of Zn 2p at the discharged/charged states. At the pristine state, there is no Zn^{2+} signal detected. When discharged to 0.2 V, two strong peaks appear at 1022 and 1045 eV, arising from the intercalation of Zn^{2+}. At the fully charged state, though becoming much weaker in intensity, these two Zn peaks can still be detected. This might originate from the surface-adsorbed Zn^{2+} salts on the electrode or the trapped Zn^{2+} ions in the lattice [32]. Fig. 6c and d presents the TEM image with the corresponding elemental mapping of NaVOH at the fully discharged and charged states. The homogeneous distribution of Zn, Na, V, and O in the discharged NaVOH confirms the uniform insertion of Zn in the structure. The detection of weaker Zn signal in the charged electrode is consistent with the XPS results (Fig. 6b). The detection of strong Na signal in both the fully discharged and charged state, revealing that the preintercalated Na^+ ions remain stable and inert in the structure upon cycling. The Na:V ratio in the charged NaVOH is estimated to be 14% from the TEM-EDS results and 13% from SEM-EDS, which does not change much with the pristine state (Na:V ~13.4%). This suggests that the preintercalated Na^+ would not be, or at least not severely, replaced by the cycled

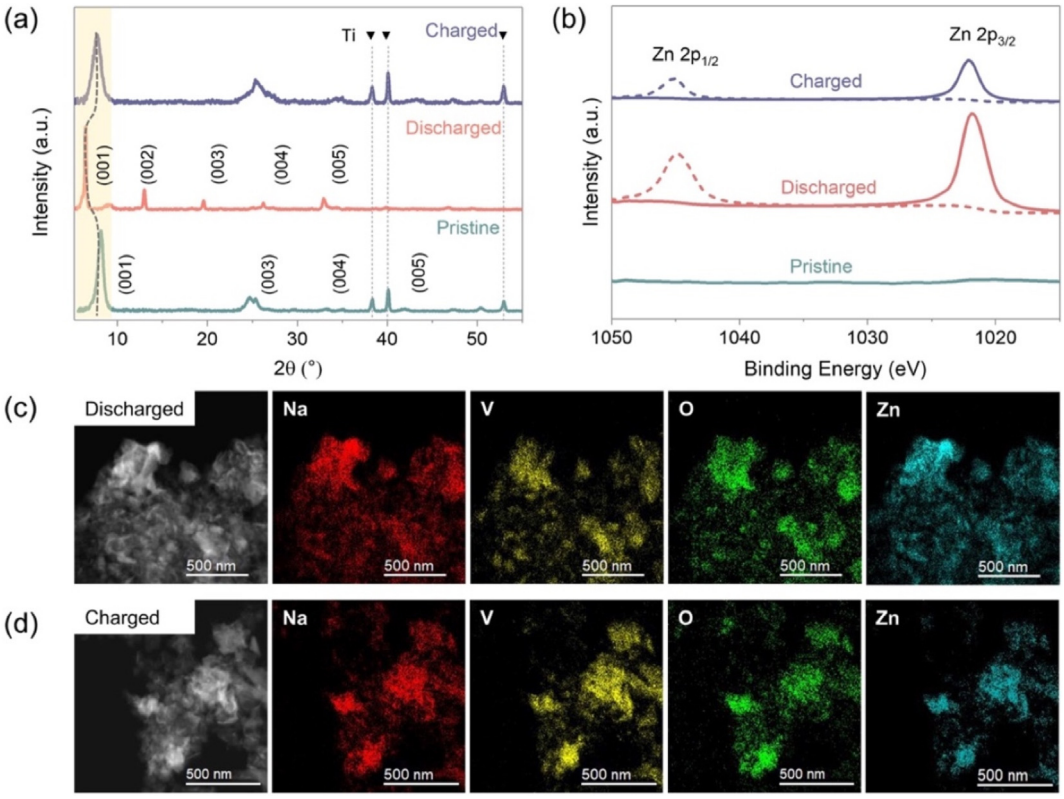

Fig. 6. (a) Ex-situ XRD patterns of NaVOH electrodes at the pristine, fully discharged and charged states (The peaks at 38, 40 and 53° comes from the titanium current collector). (b) The high resolution XPS spectra of Zn 2p of NaVOH electrodes at different states. TEM image and the corresponding EDS mappings of NaVOH at (c) the fully discharged state and (d) the fully charged state.

Zn^{2+}, which means no deterioration of the vanadium oxide network upon cycling. Though EDS is a surface analytical tool, not very precise tool to quantify the accurate element content, the comparison is still reliable. The Zn:V ratio in the discharged NaVOH is estimated to be 1.2 from SEM-EDS (Table S3), much higher than that in VOH (Zn:V~0.46). This demonstrates a two times larger amount of Zn^{2+} ions intercalating into NaVOH than VOH, supporting the higher specific capacity of NaVOH (420 mA h/g at 50 mA/g) than VOH (324 mA h/g). The above results confirm the highly stable and reversible structure of NaVOH upon Zn^{2+} intercalation/deintercalation. During discharging/charging, the original structure of NaVOH is well-maintained without obvious Na^+ ion stripping. Compared with VOH, NaVOH has the ability to uptake more Zn^{2+} ions upon discharging; the possible explanations for this are discussed in the galvanostatic intermittent titration technique (GITT) results.

2.3. Reaction and transport kinetics

CV analysis at various scan rates is carried out to explore the electrochemical reaction kinetics. As the scan rate increases from 0.1 to 1.2 mV/s (Fig. S2), the reduction and oxidation peaks shift to a lower and higher voltage, respectively, due to the enlarged polarization. The well-maintained shapes of CV curves with increased scan rates, however, indicate the facile and reversible Zn intercalation/deintercalation in NaVOH without crystallographic phase change. The peak current (i_p) obeys a power-law relationship with the scan rate v ($i_p = av^b$) [54,55]. Note that the boundary values of b are 0.5 and 1.0, corresponding to the diffusion-dominated and the capacitive-controlled current response, respectively [54,55]. For both NaVOH and VOH, the b-values of all four redox peaks lie in the middle range of 0.5–1.0 (Fig. 7a and Fig. S3), which means that the Zn^{2+} ion storage is achieved by a combination of diffusion and pseudo-capacitive-controlled process. Notice that the capacitive contribution is independent of scan rate, while the diffusion-controlled charge storage obeys a linear relationship with $v^{-1/2}$, so the contribution of each component can be separated using the following equation [54]:

$$Q\ (v) = Q_c + kv^{-1/2}$$

where Q_c represents the capacitive-controlled charge storage, $kv^{-1/2}$ quantifies the diffusion-controlled charge storage (k is a constant). By determining k, the percentage of two contributions at each scan rate can be calculated. As presented in Fig. S4, the charge storage in NaVOH is largely diffusion-controlled; even at high scan rates, diffusion process still accounts for more than 40%. But for VOH, the capacitive contribution occupies the dominant ratio at all scan rates. Another thing to note is, as the scan rate increases from 0.1 to 1.2 mV/s, the calculated diffusion contribution of NaVOH decreases slightly from 58% to 42%. The diffusion contribution of VOH, however, drops significantly from 36% to 14%. The less drop in diffusion contribution of NaVOH explains its better rate performance and suggests its enhanced ion diffusion kinetics.

It needs to be noted that, for electrode materials, the percentage of capacitive contribution makes little sense without revealing the exact capacity. To have a thorough comparison of the reaction kinetics of NaVOH and VOH, the total capacity, as well as the two types of capacity, is quantified at each scan rate. As shown in Fig. 7b, the total stored charge (per unit weight) in NaVOH is much larger than that in VOH (more than 250 C/g at 0.1 mV/s), in accordance with the higher specific capacity of NaVOH measured from GCD tests (more than 90 mA h/g at 0.05 A/g). Specifically, the capacitive-contributed capacity in NaVOH (494 C/g) is slightly lower to that in VOH (587 C/g), while the diffusion-controlled capacity in NaVOH is two times larger than that in VOH at all scan rates. This clearly reveals that the increased capacity of NaVOH is mostly provided by the diffusion-controlled process. This quantitative analysis demonstrates that NaVOH acquires less charge storage from the capacitive contribution than VOH; but it gets a sharp rise in the diffusion portion, thus enabling the total capacity to actually surpass that of VOH. The highly increased diffusion-contributed capacity of NaVOH suggests its enhanced ionic diffusion kinetics, which will be verified by the GITT results.

The smaller peak separations in CV curves, the better rate performance, a lower polarization, and higher energy efficiency of the battery with NaVOH cathode suggest that the Zn^{2+} insertion/extraction in NaVOH is much more kinetically favorable than VOH. Fig. S5 shows the Nyquist plots of NaVOH and VOH, both comprising of a depressed semicircle in the high frequency region and a sloped line in the low-frequency region (1–0.1 Hz). The diameter of the semicircle corresponds to the charge transfer resistance at the electrode/electrolyte interfaces, while the slope of the straight line is related to the ion diffusion rate in the bulk electrodes [55]. The obtained charge transfer resistance (R_{ct}) and the Zn^{2+} ion diffusion coefficient (D_{Zn}^{2+}) of NaVOH and VOH before and after cycling are listed in Table S4. Before cycling, the R_{ct} of the ZIB with VOH cathode is calculated to be 91 Ω, much larger than that of NaVOH (35 Ω). This observation agrees with our theoretical calculations that the band gap of VOH is reduced after the pre-intercalation of Na^+ions. The better electronic conductivity of NaVOH can be ascribed to its higher amount of V^{4+}, which can facilitate the hopping of unpaired electrons between V^{4+}/V^{5+}. After cycling, the R_{ct} values of both samples decrease significantly due to the gradual penetration of aqueous electrolytes. This is consistent with the capacity raising observed in the initial cycles (Figs. 5d and f). From the slope of the straight line (in the low-frequency region in Fig. S5), we can tell, before cycling, the Zn^{2+} diffusion coefficient of NaVOH is slightly smaller than that

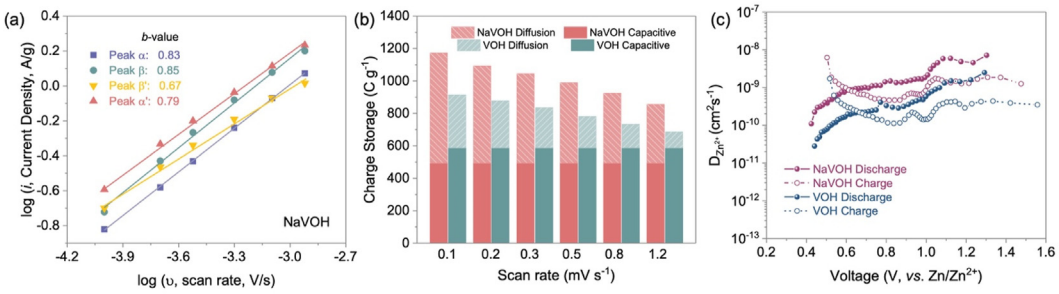

Fig. 7. Zn^{2+} ion storage kinetics of NaVOH and VOH. (a) b-values of redox peaks in CV curves (Fig. S2) of NaVOH. (b) The calculated capacitive- and diffusion-contributed capacity in NaVOH and VOH at different scan rates. (c) The diffusion coefficient of Zn^{2+} ions upon discharging/charging during the 3rd GITT cycle. CV, cyclic voltammetry; GITT, galvanostatic intermittent titration technique.

of VOH. After cycling, however, D_{Zn}^{2+} of NaVOH becomes much larger than that of VOH. The possible explanations could be, initially, the larger interlayer spacing of pristine VOH contributes to its faster ion diffusion than that of the pristine NaVOH. After cycling, however, some of the intercalated Zn^{2+} ions were trapped in the VOH structure by replacing the interlayer water. As previously stated, the partial interlayer water exist as the acid protons state (H_3O^+) in VOH, those H_3O^+ can be easily replaced by other cations or molecules [46,50]. Upon the first discharging, those H_3O^+ in VOH will be randomly substituted by the intercalated Zn^{2+} ions, hindering the subsequent Zn^{2+} migration [46]. This detrimental phenomenal can be largely avoided in NaVOH because of the stronger chemical bonds between Na^+ and the oxide network.

The change of Zn^{2+} diffusion rates upon charging/discharging was analyzed using the GITT. As shown in Fig. 7c, the calculated D_{Zn}^{2+} for VOH is in the range of 2.8×10^{-11}–2.5×10^{-9} upon discharging and 1.1×10^{-10}–1.7×10^{-9} upon charging (see calculation details in the **SI**). Even though has a narrower interlayer distance, NaVOH displays a pretty-competitive diffusion coefficient value (1.1×10^{-10} to 7.1×10^{-9} during discharging and 4.6×10^{-10} to 6.2×10^{-9} during charging), superior to VOH. This is quite different from the previous consensus that a larger interlayer spacing always leads to a faster ion diffusion, the possible explanations will be discussed later. Another observation is that D_{Zn}^{2+} during charging (deintercalation) is lower than that during discharging (intercalation), for both NaVOH and VOH. This is because the extraction of Zn^{2+} ions is more difficult than insertion due to the electrostatic interactions between the cycled ions and the host, responsible for the voltage polarization. If we compare this D_{Zn}^{2+} difference between discharge and charge processes for the two materials (Table 3), it is obvious that this difference is smaller for NaVOH than VOH, explaining the smaller voltage polarization of NaVOH observed in the CV and GCD curves. When comparing the diffusion rate change upon cycling, we can see the average D_{Zn}^{2+} of NaVOH remains highly stable; for the discharging process, there is even a 13% increase from the 1st to the 3rd cycle. The average D_{Zn}^{2+} of VOH, however, decreases 39% for the discharge process and 15% for the charge process during the first three cycles, indicating a rapid decay of ion diffusion kinetics in VOH upon cycling. Based on the above description, clearly, NaVOH displays a faster Zn^{2+} ion transportation, a smaller diffusion rate difference between charging and discharging, as well as a lower diffusion rate fluctuation upon cycling. This explains the better rate performance, smaller polarization, and slower capacity fading of NaVOH.

In summary, the intercalation of Na^+ ions and its replacement of some interlayer water in VOH generate very intricate influences on the electrochemical reaction kinetics. On one hand, due to the removal of partial structural water, the interlayer space of NaVOH shrunk, which seems to be a hindrance factor for the charge carrier diffusion. Actually, although there is a ~1 Å decrease (NaVOH: 11.0 Å, VOH: 12.0 Å), the interplanar distance of NaVOH is still more than two times larger than the radius of hydrated Zn^{2+} ions (4.3 Å [36]), wide enough for its quick transportation. In this case, when comparing the reaction kinetics of NaVOH and VOH, the role of interlayer distance is not as significant as the other limiting factors, like the structural variation during ion insertion/extraction or the electrostatic interactions between charge carriers and the host. For NaVOH, as discussed before, the preintercalated Na^+ ions form strong ionic bonds with the V–O network and remain stable in the structure upon cycling, which could help preventing the kinetics decline caused by the structure distortion. As a result, NaVOH provides the unimpeded ion diffusion channels and enables a larger amount of Zn^{2+} to diffuse deep into the inner structure without being blocked, thus exhibiting not only the promoted reaction kinetics but also a higher capacity than VOH. As for VOH, on the contrary, some of its interlayer water (H_3O^+) can be easily replaced by the inserted Zn^{2+} upon the initial discharging. The exchange of coordinated water with Zn^{2+} can occur randomly along the diffusion pathways, which not only deteriorates the V–O skeleton but also limits the migration depth of Zn^{2+} ions. So, both the cycling performance and reaction kinetics of VOH decay severely, while those of NaVOH remain highly stable.

Table 3
The calculated average Zn^{2+} diffusion coefficient for NaVOH and VOH in the first three GITT cycles.

		Zn^{2+} diffusion coefficient (D_{Zn2+}, cm^2/s)		
		1st	2nd	3rd
VOH	Discharge	7.2×10^{-10}	5.0×10^{-10}	4.4×10^{-10}
	Charge	3.4×10^{-10}	3.2×10^{-10}	2.9×10^{-10}
NaVOH	Discharge	1.5×10^{-9}	1.8×10^{-9}	1.7×10^{-9}
	Charge	1.4×10^{-9}	1.3×10^{-9}	1.2×10^{-9}

3. Conclusions

By pre-intercalating Na^+ ions into the oxide structure, about 0.3 interlayer water per V_2O_5 will be favorably replaced, leading to a decreased interlayer spacing from 12.0 Å (VOH) to 11.0 Å (δ-$Na_{0.27}V_2O_5 \cdot 0.7H_2O$, NaVOH). Though has a narrower interlayer spacing, NaVOH demonstrates a fast Zn^{2+} diffusion rate (D_{Zn}^{2+}~10^{-9}) and delivers a larger specific capacity of 420 mA h/g (at 0.05 A/g), an improved energy efficiency (88% at 0.05 A/g) with a higher Zn^{2+} intercalation/deintercalation reversibility, and a significantly improved electrochemical stability (88% capacity retention after 2000 cycles at 4 A/g), in comparison to those of VOH. These observations are different from many previous works that pre-intercalation foreign species will always expand the lattice spacing of VOH, and the bigger interlayer distance accounts for the improved electrochemical reversibility and stability. The interplanar distance of $M_xV_2O_5 \cdot nH_2O$ (M: preintercalated metal cations) depend on both the amount of interlayer water and the types of pre-inserted M cations. A higher interlayer water content, a larger hydrated ion radius, and a bigger electronegativity of M (smaller electronegativity difference between M and oxygen) give $M_xV_2O_5 \cdot nH_2O$ a wider interplanar space. The understandings about how the Na^+pre-intercalation affect the crystal structure and the electrochemical performance are first, Na^+ ions can be pre-intercalated into VOH via replacing partial interlayer water; this results in a decreased basal distance, a reduced structural water content, and an increased V^{4+} amount in NaVOH. Second, the introduction of more V^{4+} can facilitate the hopping of electrons between V^{4+} and V^{5+}, hence enhancing the electronic conductivity. Third, the replacement of partial interlayer water by Na^+ions could alleviate the interactions between cycled Zn^{2+} ions and the host, which ensures a faster and more reversible Zn^{2+} ion insertion/extraction without server structural distortion. As for the VOH, its structural water (those exist in the form of H_3O^+) can be readily and randomly replaced by Zn^{2+} ions upon discharging, blocking the pathways for the subsequent Zn^{2+} migration. So, both the cycling performance and kinetics properties of VOH decay severely upon cycling. This work not only highlights the versatility of pre-intercalating metal ions into the bilayered vanadium oxides but also reveals its effects on the interlayer spacing, structural stability, and the overall electrochemical performance.

Credit author statement

Xiaoxiao Jia: Methodology, Investigation, Formal analysis, Writing-Original draft preparation, Writing-Reviewing and Editing.

Ruixue Tian: Software, Validation, Writing-Reviewing and Editing. **Chaofeng Liu**: Conceptualization, Methodology, Investigation, Writing-Reviewing and Editing. **Jiqi Zheng**: Investigation. **Meng Tian**: Investigation. **Guozhong Cao:** Supervision, Writing-Reviewing and Editing.

Declaration of competing interest

The authors declare that they have no known competing financial interests or personal relationships that could have appeared to influence the work reported in this paper.

Acknowledgments

This work was supported by the National Science Foundation [CBET-1803256]. The author acknowledges the financial support from the Clean Energy Institute Graduate Fellowship at the University of Washington.

Appendix A. Supplementary data

Supplementary data to this article can be found online at https://doi.org/10.1016/j.mtener.2022.101063.

References

[1] D. Larcher, J.M. Tarascon, Towards greener and more sustainable batteries for electrical energy storage, Nat. Chem. 7 (2014) 19, https://doi.org/10.1038/nchem.2085.
[2] C. Hou, Q. Xu, Metal–organic frameworks for energy, Adv. Energy Mater. 9 (2019) 1801307, https://doi.org/10.1002/aenm.201801307.
[3] Z. Liu, L. Qin, B. Lu, X. Wu, S. Liang, J. Zhou, Issues and opportunities facing aqueous Mn^{2+}/MnO_2-based batteries, ChemSusChem 15 (2022), e202200348, https://doi.org/10.1002/cssc.202200348.
[4] C. Li, C. Hou, L. Chen, S. Kaskel, Q. Xu, Rechargeable Al-ion batteries, EnergyChem 3 (2021) 100049, https://doi.org/10.1016/j.enchem.2020.100049.
[5] B. Tang, L. Shan, S. Liang, J. Zhou, Issues and opportunities facing aqueous zinc-ion batteries, Energy Environ. Sci. 12 (2019) 3288–3304, https://doi.org/10.1039/C9EE02526J.
[6] X. Jia, C. Liu, Z.G. Neale, J. Yang, G. Cao, Active materials for aqueous zinc ion batteries: synthesis, crystal structure, morphology, and electrochemistry, Chem. Rev. 120 (2020) 7795–7866, https://doi.org/10.1021/acs.chemrev.9b00628.
[7] P. Ruan, S. Liang, B. Lu, H.J. Fan, J. Zhou, Design strategies for high-energy-density aqueous zinc batteries, Angew. Chem. Int. Ed. 61 (2022), e202200598, https://doi.org/10.1002/anie.202200598.
[8] C. Zhu, G. Fang, S. Liang, Z. Chen, Z. Wang, J. Ma, H. Wang, B. Tang, X. Zheng, J. Zhou, Electrochemically induced cationic defect in MnO intercalation cathode for aqueous zinc-ion battery, Energy Storage Mater. 24 (2020) 394–401, https://doi.org/10.1016/j.ensm.2019.07.030.
[9] H. Yang, W. Zhou, D. Chen, J. Liu, Z. Yuan, M. Lu, L. Shen, V. Shulga, W. Han, D. Chao, The origin of capacity fluctuation and rescue of dead Mn-based Zn–ion batteries: a Mn-based competitive capacity evolution protocol, Energy Environ. Sci. 15 (2022) 1106–1118, https://doi.org/10.1039/D1EE03547A.
[10] G. Kasiri, J. Glenneberg, A. Bani Hashemi, R. Kun, F. La Mantia, Mixed copper-zinc hexacyanoferrates as cathode materials for aqueous zinc-ion batteries, Energy Storage Mater. 19 (2019) 360–369, https://doi.org/10.1016/j.ensm.2019.03.006.
[11] L. Zhang, L. Chen, X. Zhou, Z. Liu, Towards high-voltage aqueous metal-ion batteries beyond 1.5 V: the zinc/zinc hexacyanoferrate system, Adv. Energy Mater. 5 (2014) 1400930, https://doi.org/10.1002/aenm.201400930.
[12] H. Kobayashi, K. Oizumi, T. Tomai, I. Honma, Graphene and polyethyleneimine bilayer wrapping onto quinone molecular crystal cathode materials for aqueous zinc-ion batteries, ACS Appl. Energy Mater. 5 (2022) 4707–4711, https://doi.org/10.1021/acsaem.2c00134.
[13] K.W. Nam, H. Kim, Y. Beldjoudi, T. Kwon, D.J. Kim, J.F. Stoddart, Redox-active phenanthrenequinone triangles in aqueous rechargeable zinc batteries, J. Am. Chem. Soc. 142 (2020) 2541–2548, https://doi.org/10.1021/jacs.9b12436.
[14] C. Xia, J. Guo, P. Li, X.X. Zhang, H.N. Alshareef, Highly stable Aqueous zinc-ion storage using a layered calcium vanadium oxide bronze cathode, Angew. Chem. Int. Ed. 57 (2018) 3943–3948, https://doi.org/10.1002/anie.201713291.
[15] B. Tang, G. Fang, J. Zhou, L. Wang, Y. Lei, C. Wang, T. Lin, Y. Tang, S. Liang, Potassium vanadates with stable structure and fast ion diffusion channel as cathode for rechargeable aqueous zinc-ion batteries, Nano Energy 51 (2018) 579–587, https://doi.org/10.1016/j.nanoen.2018.07.014.
[16] N. Zhang, M. Jia, Y. Dong, Y. Wang, J. Xu, Y. Liu, L. Jiao, F. Cheng, Hydrated layered vanadium oxide as a highly reversible cathode for rechargeable aqueous zinc batteries, Adv. Funct. Mater. 29 (2019) 1807331, https://doi.org/10.1002/adfm.201807331.
[17] P. He, G.B. Zhang, X.B. Liao, M.Y. Yan, X. Xu, Q.Y. An, J. Liu, L.Q. Mai, Sodium ion stabilized vanadium oxide nanowire cathode for high-performance zinc-ion batteries, Adv. Energy Mater. 8 (2018), https://doi.org/10.1002/aenm.201702463.
[18] B. Sambandam, V. Soundharrajan, S. Kim, M.H. Alfaruqi, J. Jo, S. Kim, V. Mathew, Y.K. Sun, J. Kim, Aqueous rechargeable Zn-ion batteries: an imperishable and high-energy $Zn_2V_2O_7$ nanowire cathode through intercalation regulation, J. Mater. Chem. 6 (2018) 3850–3856, https://doi.org/10.1039/c7ta11237h.
[19] L. Shan, Y. Wang, S. Liang, B. Tang, Y. Yang, Z. Wang, B. Lu, J. Zhou, Interfacial adsorption–insertion mechanism induced by phase boundary toward better aqueous Zn-ion battery, InfoMat 3 (2021) 1028–1036, https://doi.org/10.1002/inf2.12223.
[20] D. Chen, M. Lu, B. Wang, H. Cheng, H. Yang, D. Cai, W. Han, H.J. Fan, High-mass loading $V_3O_7{\cdot}H_2O$ nanoarray for Zn-ion battery: new synthesis and two-stage ion intercalation chemistry, Nano Energy 83 (2021) 105835, https://doi.org/10.1016/j.nanoen.2021.105835.
[21] H. Liang, Z. Cao, F. Ming, W. Zhang, D.H. Anjum, Y. Cui, L. Cavallo, H.N. Alshareef, Aqueous zinc-ion storage in MoS_2 by tuning the intercalation energy, Nano Lett. 19 (2019) 3199–3206, https://doi.org/10.1021/acs.nanolett.9b00697.
[22] H. Li, Q. Yang, F. Mo, G. Liang, Z. Liu, Z. Tang, L. Ma, J. Liu, Z. Shi, C. Zhi, MoS_2 nanosheets with expanded interlayer spacing for rechargeable aqueous Zn-ion batteries, Energy Storage Mater. 19 (2019) 94–101, https://doi.org/10.1016/j.ensm.2018.10.005, 2018.
[23] X. Li, L. Ma, Y. Zhao, Q. Yang, D. Wang, Z. Huang, G. Liang, F. Mo, Z. Liu, C. Zhi, Hydrated hybrid vanadium oxide nanowires as the superior cathode for aqueous Zn battery, Mater, Today Energy 14 (2019) 100361, https://doi.org/10.1016/j.mtener.2019.100361.
[24] J. Livage, Interface properties of vanadium pentoxide gels, Mater. Res. Bull. 26 (1991) 1173–1180, https://doi.org/10.1016/0025-5408(91)90123-4.
[25] Y. Oka, N. Yamamoto, T. Yao, Ion-exchange properties of hydrated vanadium oxide with a layered structure of alkali-metal ions, Solid State Ion 57 (1992) 103–107, https://doi.org/10.1016/0167-2738(92)90070-6.
[26] H.H. Kristoffersen, H. Metiu, Structure of $V_2O_5{\cdot}nH_2O$ xerogels, J. Phys. Chem. C 120 (2016) 3986–3992, https://doi.org/10.1021/acs.jpcc.5b12418.
[27] C. Liu, M. Tian, M. Wang, J. Zheng, S. Wang, M. Yan, Z. Wang, Z. Yin, J. Yang, G. Cao, Catalyzing zinc-ion intercalation in hydrated vanadates for aqueous zinc-ion batteries, J. Mater. Chem. 8 (2020) 7713–7723, https://doi.org/10.1039/D0TA01468K.
[28] M. Tian, C. Liu, J. Zheng, X. Jia, E.P. Jahrman, G.T. Seidler, D. Long, M. Atif, M. Alsalhi, G. Cao, Structural engineering of hydrated vanadium oxide cathode by K^+ incorporation for high-capacity and long-cycling aqueous zinc ion batteries, Energy Storage Mater. 29 (2020) 9–16, https://doi.org/10.1016/j.ensm.2020.03.024.
[29] J. Zheng, C. Liu, M. Tian, X. Jia, E.P. Jahrman, G.T. Seidler, S. Zhang, Y. Liu, Y. Zhang, C. Meng, G. Cao, Fast and reversible zinc ion intercalation in Al-ion modified hydrated vanadate, Nano Energy 70 (2020) 104519, https://doi.org/10.1016/j.nanoen.2020.104519.
[30] S. Tepavcevic, H. Xiong, V.R. Stamenkovic, X. Zuo, M. Balasubramanian, V.B. Prakapenka, C.S. Johnson, T. Rajh, Nanostructured bilayered vanadium oxide electrodes for rechargeable sodium-ion batteries, ACS Nano 6 (2012) 530–538, https://doi.org/10.1021/nn203869a.
[31] Q. Xie, G. Cheng, T. Xue, L. Huang, S. Chen, Y. Sun, M. Sun, H. Wang, L. Yu, Alkali ions pre-intercalation of δ-MnO_2 nanosheets for high-capacity and stable Zn-ion battery, Mater, Today Energy 24 (2022) 100934, https://doi.org/10.1016/j.mtener.2021.100934.
[32] C. Liu, Z. Neale, J. Zheng, X. Jia, J. Huang, M. Yan, M. Tian, M. Wang, J. Yang, G. Cao, Expanded hydrated vanadate for high-performance aqueous zinc-ion batteries, Energy Environ. Sci. 12 (2019) 2273–2285, https://doi.org/10.1039/C9EE00956F.
[33] M. Clites, E. Pomerantseva, Bilayered vanadium oxides by chemical pre-intercalation of alkali and alkali-earth ions as battery electrodes, Energy Storage Mater. 11 (2018) 30–37, https://doi.org/10.1016/j.ensm.2017.09.005.
[34] A. Moretti, S. Passerini, Bilayered nanostructured $V_2O_5{\cdot}nH_2O$ for metal batteries, Adv. Energy Mater. 6 (2016) 1600868, https://doi.org/10.1002/aenm.201600868.
[35] Y. Yang, Y. Tang, G. Fang, L. Shan, J. Guo, W. Zhang, C. Wang, L. Wang, J. Zhou, S. Liang, Li^+ intercalated $V_2O_5{\cdot}nH_2O$ with enlarged layer spacing and fast ion diffusion as an aqueous zinc-ion battery cathode, Energy Environ. Sci. 11 (2018) 3157–3162, https://doi.org/10.1039/C8EE01651H.
[36] X. Buenaño, L. Canoira, D. Martin Sánchez, J. Costafreda, Zeolitic tuffs for acid mine drainage (AMD) treatment in Ecuador: breakthrough curves for Mn^{2+}, Cd^{2+}, Cr^{3+}, Zn^{2+}, and Al^{3+}, Environ. Sci. Pollut. Res. 24 (2017) 6794–6806, https://doi.org/10.1007/s11356-016-8177-9.
[37] H. Ashjian, Q.N. Le, D.O. Marler, J. Shim, S.S. Wong, Naphthalene Alkylation Process, Patent Cooperation Treaty, 1991. WO1991015443A1, October 17, https://patents.google.com/patent/WO1991015443A1/en.
[38] J. Emsley, The Elements, third ed., Clarendon Press, Oxford, 1998.
[39] S.-H. Lee, H.M. Cheong, M.J. Seong, P. Liu, C.E. Tracy, A. Mascarenhas, J.R. Pitts, S.K. Deb, Raman spectroscopic studies of amorphous vanadium oxide thin films, Solid State Ion 165 (2003) 111–116, https://doi.org/10.1016/j.ssi.2003.08.022.

[40] S. Boukhalfa, K. Evanoff, G. Yushin, Atomic layer deposition of vanadium oxide on carbon nanotubes for high-power supercapacitor electrodes, Energy Environ. Sci. 5 (2012) 6872–6879, https://doi.org/10.1039/C2EE21110F.
[41] C. Sanchez, J. Livage, G. Lucazeau, Infrared and Raman study of amorphous V_2O_5, J. Raman Spectrosc. 12 (1982) 68–72, https://doi.org/10.1002/jrs.1250120110.
[42] J. Lee, S. Badie, P. Srimuk, A. Ridder, H. Shim, S. Choudhury, Y.-C. Nah, V. Presser, Electrodeposition of hydrated vanadium pentoxide on nanoporous carbon cloth for hybrid energy storage, Sustain. Energy Fuels 2 (2018) 577–588, https://doi.org/10.1039/C7SE00559H.
[43] M. Clites, Chemical Pre-intercalation Synthesis Approach for Novel Layered Cathode Materials for Li-Ion and beyond Li-Ion Batteries, Ph D. Thesis, Drexel University, 2019.
[44] W. Chen, L. Mai, J. Peng, Q. Xu, Q. Zhu, Raman spectroscopic study of vanadium oxide nanotubes, J. Solid State Chem. 177 (2004) 377–379, https://doi.org/10.1016/S0022-4596(03)00416-X.
[45] C. Londoño-Calderón, C. Vargas-Hernández, J. Jurado, Desorption influence of water on structural, electrical properties and molecular order of vanadium pentoxide xerogel films, Rev. Mexic. Fisica 56 (2010) 411–415.
[46] J. Livage, Vanadium pentoxide gels, Chem. Mater. 3 (1991) 578–593, https://doi.org/10.1021/cm00016a006.
[47] W. Avansi Jr., C. Ribeiro, E.R. Leite, V.R. Mastelaro, Vanadium pentoxide nanostructures: an effective control of morphology and crystal structure in hydrothermal conditions, Cryst. Growth Des. 9 (2009) 3626–3631, https://doi.org/10.1021/cg900373f.
[48] P. Aldebert, N. Baffier, N. Gharbi, J. Livage, Layered structure of vanadium pentoxide gels, Mater. Res. Bull. 16 (1981) 669–676, https://doi.org/10.1016/0025-5408(81)90266-X.
[49] J. Livage, Optical and electrical properties of vanadium oxides synthesized from alkoxides, Coord. Chem. Rev. 190–192 (1999) 391–403, https://doi.org/10.1016/S0010-8545(99)00096-X.
[50] G.S. Zakharova, V.L. Volkov, Intercalation compounds based on vanadium(V) oxide xerogel, Russ. Chem. Rev. 72 (2003) 311–325, https://doi.org/10.1070/RC2003v072n04ABEH000762.
[51] A. Benayad, H. Martinez, A. Gies, B. Pecquenard, A. Levasseur, D. Gonbeau, XPS investigations achieved on the first cycle of V_2O_5 thin films used in lithium microbatteries, J. Electron. Spectrosc. Relat. Phenom. 150 (2006) 1–10, https://doi.org/10.1016/j.elspec.2005.09.001.
[52] J. Livage, Synthesis of polyoxovanadates via “chimie douce”, Coord. Chem. Rev. 178–180 (1998) 999–1018, https://doi.org/10.1016/S0010-8545(98)00105-2.
[53] A. Eftekhari, Energy efficiency: a critically important but neglected factor in battery research, Sustain, Energy Fuels 1 (2017) 2053–2060, https://doi.org/10.1039/C7SE00350A.
[54] J. Liu, J. Wang, C. Xu, H. Jiang, C. Li, L. Zhang, J. Lin, Z.X. Shen, Advanced energy storage devices: basic principles, analytical methods, and rational materials design, Adv. Sci. 5 (2018) 1700322, https://doi.org/10.1002/advs.201700322.
[55] X. Yang, A.L. Rogach, Electrochemical techniques in battery research: a tutorial for nonelectrochemists, Adv. Energy Mater. 9 (2019) 1900747, https://doi.org/10.1002/aenm.201900747.